Research Article

Nano Research
2020, 13(3): 818–823

ISSN 1998-0124 CN 11-5974/O4
https://doi.org/10.1007/s12274-020-2702-3

# ZIF-8/$LiFePO_4$ derived Fe-N-P Co-doped carbon nanotube encapsulated $Fe_2P$ nanoparticles for efficient oxygen reduction and Zn-air batteries

Huihui Jin[1], Huang Zhou[1], Pengxia Ji[1], Chengtian Zhang[1], Jiahuan Luo[1,3], Weihao Zeng[1], Chenxi Hu[1], Daping He[1,2] (✉), and Shichun Mu[1] (✉)

[1] *State Key Laboratory of Advanced Technology for Materials Synthesis and Processing, Wuhan University of Technology, Wuhan 430070, China*
[2] *Hubei Engineering Research Center of RF-Microwave Technology and Application, Wuhan University of Technology, Wuhan 430070, China*
[3] *Department of Chemical and Environmental Engineering, Anyang Institute of Technology, Anyang 455000, China*


**Received:** 30 November 2019 / **Revised:** 18 January 2020 / **Accepted:** 6 February 2020

## ABSTRACT

Iron-based oxygen reduction reaction (ORR) catalysts have been the focus of research, and iron sources play an important role for the preparation of efficient ORR catalysts. Here, we successfully use $LiFePO_4$ as ideal sources of Fe and P to construct the heteroatom doped Fe-based carbon materials. The obtained Fe-N-P co-doped coral-like carbon nanotube arrays encapsulated $Fe_2P$ catalyst (C-ZIF/LFP) shows very high half-wave potential of 0.88 V in alkaline electrolytes toward ORR, superior to Pt/C (0.85 V), and also presents a high half-wave potential of 0.74 V in acidic electrolytes, comparable to Pt/C (0.8 V). When further applied into a home-made Zn-air battery as cathode, a peak power density of 140 $mW{\cdot}cm^{-2}$ is reached, exceeds commercial Pt/C (110 $mW{\cdot}cm^{-2}$). Besides, it also presents exceptional durability and methanol resistance compared with Pt/C. Noticeably, the preparation method of such a high-performance catalyst is simple and easy to optimize, suitable for the large-scale production. What's more, it opens up a more sustainable development scenario to reduce the hazardous wastes such as $LiFePO_4$ by directly using them for preparing high-performance ORR catalysts.

## KEYWORDS

$LiFePO_4$, waste utilization, ZIF-8, heteroatoms-doped, oxygen reduction reaction

## 1 Introduction

Under the basic principle of sustainable development, fuel cells including metal-air batteries have become a research hotspot in the energy field, but their commercialization are constrained by the sluggish cathodic reaction (oxygen reduction reaction, ORR) kinetics and high catalysts cost [1, 2]. Although noble materials (Pt, Pd, etc.) have extremely high catalytic efficiency for ORR, the deficiencies of limited reserves, high prices and vulnerability to poisoning seriously hinder their commercial applications [3, 4]. Therefore, Pt-free catalysts with high catalytic activity, stability and resistance to methanol poisoning have to be explored.

For non-precious metal catalysts (NPMCs), early theoretical and experimental studies have presented C-N groups can serve as highly active centers for oxygen reduction [5–9]. Compared with other heteroatoms, nitrogen (N) atoms have abundant implantable sites in carbon structure and can produce many types of C-N structures, so N-doped carbon materials have become the most promising non-metallic doping materials [10, 11]. Furthermore, current studies have shown that incorporating transition metal moieties in C-N structures to form M-N-C system can further enhance the ORR activity of non-precious metal catalysts [12–14]. Among them, iron-based carbon materials (Fe-N-C) have desirable performance in oxygen reduction electrocatalysis [15–19]. However, though iron resources are rich in the earth, the exploitation and synthesis of new iron compounds still require the consumption of energy. Thus, one of the best approaches is to reuse the iron-containing compounds that have been used up and even discarded, such as materials in lithium ion batteries.

Especially, with the rapid development of power batteries, the battery system with $LiFePO_4$ as the mainstream will lead to the production of a large amount of hazardous waste in the future. Therefore, the direct use of $LiFePO_4$ for preparing other functional materials can be beneficial to alleviate the environmental pressure generated by them, and bring considerable economic benefits. Besides, $LiFePO_4$ is not only rich in iron source, but also has abundant phosphorus (P) atoms which are favorable for oxygen reduction. Undoubtedly, $LiFePO_4$ is an ideal raw material for preparing oxygen reduction materials. In addition, metal-organic framework (MOF) is a material constituted by connecting organic ligands with inorganic metal ions (or metal clusters) through coordination bonds. MOF constructed with N-containing heterocyclic ligands contains generous uncoordinated nitrogen atoms in the framework, providing a rich N source to form C-N and M-N active sites for ORR after carbonization [20–28].

Address correspondence to Shichun Mu, msc@whut.edu.cn; Daping He, hedaping@whut.edu.cn

As a result, with using a nitrogen-rich zeolitic imidazolate framework (ZIF-8) as carbon and nitrogen sources, and $LiFePO_4$ as iron and phosphorous sources, we create a simplest method to prepare a highly active oxygen reduction catalyst. Since the Fe and P atoms provided by $LiFePO_4$ and N atoms provided by ZIF-8 could be mutually co-doped into the carbon framework, the obtained material (C-ZIF/LFP) has an outstanding ORR performance under both alkaline and acidic electrolytes. Moreover, a Zn-air battery with C-ZIF/LFP as the cathode exhibits higher peak power density and discharge voltage than commercial Pt/C.

## 2 Experimental

### 2.1 Catalyst synthesis

ZIF-8 was prepared by stirring a methanol solution containing $Zn(NO_3)_2{\cdot}9H_2O$ and 2-methylimidazole for 4 h at 36 °C. The prepared ZIF-8 (300 mg) was mixed with commercial $LiFePO_4$ (50 mg) and ground. The mixture (ZIF/LFP) was then calcined in a tube furnace at different temperatures (800, 900, and 1,000 °C) for different times (2, 3, and 4 h) under $N_2$ protection. The as-prepared catalyst was named as C-ZIF/LFP-*X*-3 h (*X* represents pyrolyzing temperature) or C-ZIF/LFP-900-*Y* h (*Y* represents pyrolyzing time). C-ZIF/LFP-900-3 h also referred to as C-ZIF/LFP for short. C-ZIF and C-LFP were obtained by treating pure ZIF-8 and $LiFePO_4$ at 900 °C for 3 h under $N_2$ protection, respectively. C-C/LFP and C-C-ZIF/LFP were prepared under the same calcination treatment by calcining the mixture of conductive carbon (30 mg) and $LiFePO_4$ (30 mg), and the mixture of C-ZIF (30 mg) and $LiFePO_4$ (30 mg), respectively.

### 2.2 Electrochemical measurements

The electrochemical tests were carried out on the electrochemical workstation (CHI 760E) based on the three-electrode model, including counter electrode (platinum wire), reference electrode (calibrated Ag/AgCl electrode filled with saturated potassium chloride in alkaline conditions or saturated calomel electrode (SCE) in acidic conditions, which can be converted to reversible hydrogen electrode (RHE) scale using the Nernst equation) and working electrode (rotating disk electrode (RDE) or a rotating ring disk electrode (RRDE) coated with catalyst ink (20 μL for as-synthesized sample ink, 10 μL for commercial Pt/C)). The catalyst ink was prepared by dispersing 5 mg of catalyst in a solution consisting of 900 μL of isopropanol, 100 μL of deionized water and 20 μL of Nafion (5%), and ultrasonically treated to a uniform ink.

### 2.3 Fabrication of primary Zn-air battery

*Liquid Zn-air battery:* The anode is zinc foil, cathode is carbon paper coated with catalyst (1 mg·cm$^{-2}$), and the liquid electrolyte is the mixture solution of 6.0 M potassium hydroxide and 0.2 M zinc acetate.

*All solid-state Zn-air battery:* The anode is zinc foil, cathode is nickel mesh supported by catalyst, the solid electrolyte is a PVA film. The preparation of polyvinyl alcohol (PVA) film was as follows: 4.5 g PVA powder was added to 45 mL $H_2O$ containing 0.1 M potassium hydroxide and 0.02 M zinc acetate. The mixture was further stirred at 90 °C to form a transparent gel, then the gel was wobbled into a film in petri dish and frozen in refrigerator.

## 3 Results and discussion

By investigation of different calcination temperatures and times, we firstly found that the sample after calcination at 900 °C for 3 h in protective atmosphere had the best ORR activity (Figs. S1 and S2 in the Electronic Supplementary Material (ESM)). Figure 1 depicts the preparation process of C-ZIF/LFP. The prepared ZIF-8 (300 mg) and the purchased commercial $LiFePO_4$ (LFP) (50 mg) were mixed and ground, and the obtained precursor (ZIF/LFP) was then held at 900 °C for 3 h in $N_2$ environment to synthesize C-ZIF/LFP. Pure ZIF-8 and pure $LiFePO_4$ were also held at 900 °C for 3 h, named as C-ZIF and C-LFP, respectively.

From scanning electron microscopy (SEM) and X-ray diffraction (XRD) results in Figs. S3 and S4 in the ESM, ZIF/LFP obtained by physical mixture of ZIF-8 and $LiFePO_4$ has no obvious chemical change. After calcination at 900 °C for 3 h, ZIF/LFP was transformed into a carbon material (C-ZIF/LFP) containing $LiFePO_4$ and $Fe_2P$ (Fig. 2(a)). Among them, $Fe_2P$ has been proved to be able to assist other catalytically active sites in promoting the catalytic process [29–31]. Due to the interatomic recombination between ZIF-8 and $LiFePO_4$, the morphology of C-ZIF/LFP became a coral-like carbon nanotube (CNT) array (Fig. S5 in the ESM).

The TEM image reveals that the diameter of CNT in C-ZIF/LFP ranges from 100 to 150 nm, and their tube walls are of loose-packed carbon layers, differing from the common-closed multi-walled CNT. In addition, some nanoparticles with different sizes are clearly visible in CNT (Figs. 2(b) and 2(c)). Furthermore, the high-resolution observations of the local area selected on the inside particle show that the particle has an interplanar spacing of 0.169 nm (Fig. 2(c)(1)) and 0.507 nm (Fig. 2(c)(2)),

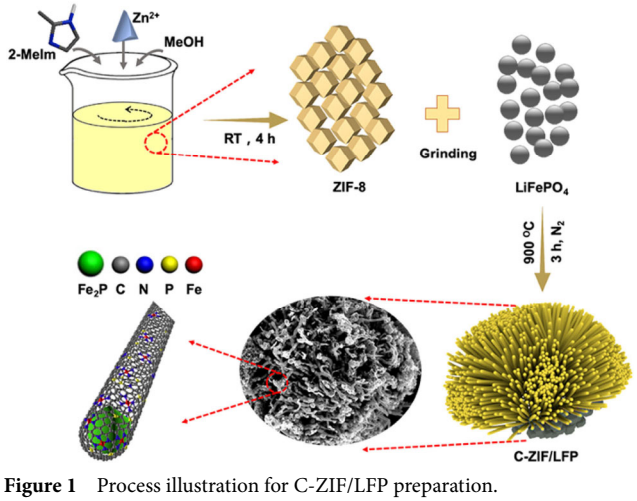


**Figure 1** Process illustration for C-ZIF/LFP preparation.

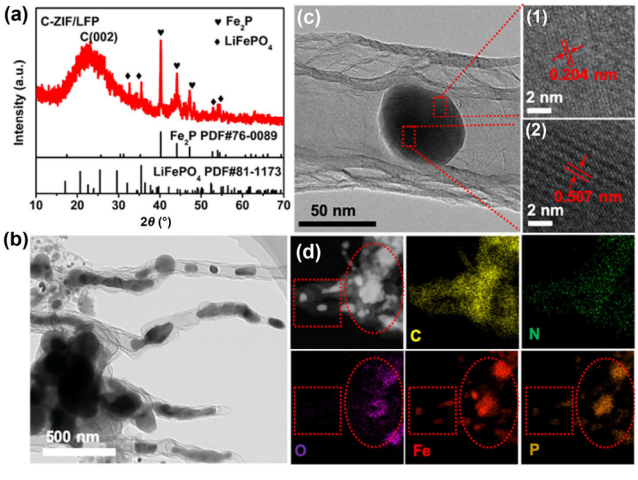


**Figure 2** (a) XRD pattern, (b) TEM, (c) high-resolution TEM (HRTEM) (1) and (2) images, and (d) EDX mapping of C-ZIF/LFP.

corresponding to the (300) plane and the (100) plane of $Fe_2P$, respectively. In further energy-dispersive X-ray spectroscopy (EDX) mapping diagrams (Fig. 2(d)), the inside particles are only covered by Fe and P, while the outside particles are covered with additional O, which can be concluded that the inside and outside particles are $Fe_2P$ and $LiFePO_4$, respectively.

As shown in Fig. 3(a), the diffraction peaks of C-LFP is well matched with $LiFePO_4$, illustrating that pure $LiFePO_4$ can ensure the phase stability at high temperatures under the protection of $N_2$. However, through thermogravimetric analysis, the obvious endothermic peak in the differential scanning calorimetry (DSC) curve of ZIF/LFP at the temperature above 600 °C implies that $LiFePO_4$ begins to melt, at which point the mass of ZIF/LFP begins decrease substantially, indicating that ZIF-8 is undergoing decomposition (Fig. S6 in the ESM). Consequently, during the reaction, part of iron atoms in the molten $LiFePO_4$ are captured by ZIF-8 converted carbon-nitrogen materials, and the remaining elements are recombined to produce new substances ($Fe_2P$). Lastly, some unreacted $LiFePO_4$ is retained in the final product, which agrees well with the results of Fig. 2(a). The formation of new phase and the change of morphology will inevitably affect the carbon structure, as suggested by the Raman spectra of C-ZIF/LFP and C-ZIF. As presented in Fig. 3(b), there are mainly two characteristic carbon peaks, namely D band (around 1,300 $cm^{-1}$) and G band (around 1,580 $cm^{-1}$), representing the disordered structure of carbon atom crystals and the $sp^2$ structure of carbon, respectively [32, 33]. The $I_D/I_G$ of C-ZIF/LFP (1.07) is significantly higher than that of C-ZIF (1.03), implying that the carbon structure in C-ZIF/LFP possesses more defects.

In the C1s XPS spectra, five typical carbon peaks are located at 284.5, 285, 286.2, 286.6, and 288.1 eV, referring to C-$sp^2$, C-$sp^3$, C–N, C–O, and C=O, respectively (Fig. 3(c)) [34, 35]. Compared to the carbon peaks of C-ZIF, a rising C–N peak, serving as an oxygen reduction active site, can be observed in C-ZIF/LFP, which is attributed to the presence of iron [36]. In addition, the N atom coordinated with C atom can be split into three types: pyridinic N (pyri-N, 398.4 eV), pyrrolic N (pyrr-N, 399.9 eV) and graphitic N (grap-N, 401.1 eV) [37, 38]. According to the previous literature, graphitic N can elevate the ORR limiting current density [39, 40], while pyridinic N is beneficial to increase the onset potential, and Fe atom is prone to coordinating with pyridinic N to produce Fe–N structure and work with C–N to catalyze oxygen reduction [41, 42]. Remarkably, after the reaction between ZIF-8 and $LiFePO_4$, the pyridinic N content of C-ZIF/LFP is almost unchanged, but the graphitic N content is obviously increased, and the Fe–N (399.2 eV) structure is formed at the same time (Fig. 3(d)). Moreover, the P atoms in C-ZIF/LFP have three forms of composition, as shown by the P2p spectrum in Fig. 3(e). The peaks at 129.1 and 130.2 eV represent $P2p_{3/2}$ and $P2p_{1/2}$, respectively, which are caused by the bonding of metal and phosphorus, and the peak located at 133.1 eV represents C–P–O, which means that some P atoms are doped into the carbon framework, while the peak located at 134 eV represents C–O–P [43–45], which may come from the P atom in the undecomposed $LiFePO_4$ adjacent to the carbon framework. Coincidently, similarly to N atoms, P atoms with stronger electronegativity have been proved to be beneficial for regulating the electronic structure of carbon [46, 47]. The high-resolution Fe2p spectrum of C-ZIF/LFP contains four peaks, namely Fe(II)$2p_{3/2}$ (710 eV), Fe(III)$2p_{3/2}$ (714.6 eV), Fe(II)$2p_{1/2}$ (723.6 eV) and Fe(III)$2p_{1/2}$ (725.6 eV) (Fig. 3(f)), implying Fe is in a mixed valence state in C-ZIF/LFP. Since no peak can be separated at 708 eV, no metal iron or iron carbide is generated in C-ZIF/LFP.

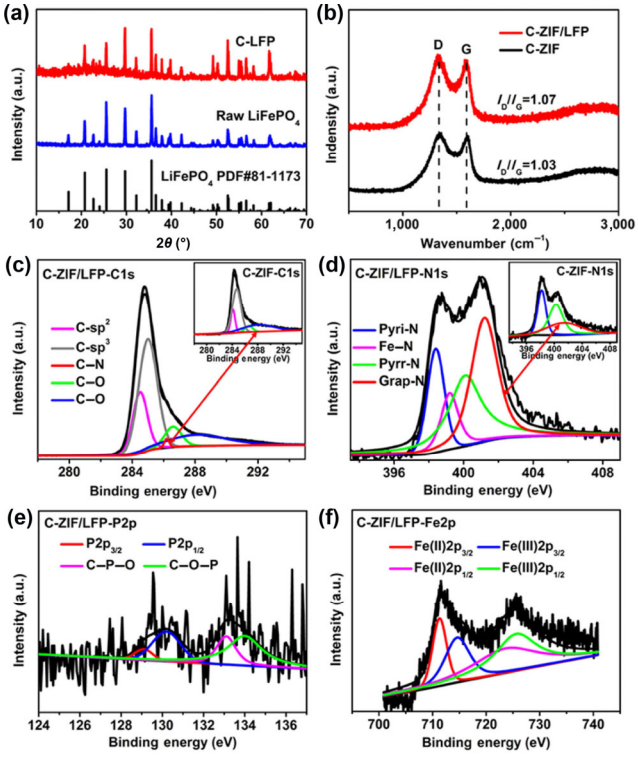


**Figure 3** (a) XRD patterns of raw $LiFePO_4$ and C-LFP; (b) Raman spectra, (c) C1s XPS, and (d) N1s XPS of C-ZIF/LFP and C-ZIF; (e) P2p spectrum and (f) Fe2p spectrum of C-ZIF/LFP.

Inspired by the unique coral-like CNT structure of C-ZIF/LFP and the heteroatoms (N, P) doping that favors oxygen reduction, the ORR performance of C-ZIF/LFP was evaluated under both alkaline and acidic conditions. Firstly, by cyclic voltammetry (CV) curves tested under alkaline, the electrolytes filled with oxygen, C-ZIF/LFP displays a distinct oxygen reduction peak (Fig. S7 in the ESM), indicating that it is able to reduce oxygen. Then, the linear sweep voltammetry (LSV) curves (Figs. 4(a) and 4(b)) reveal that C-ZIF/LFP possesses an onset potential ($E_{onset}$) of 0.98 V and a half-wave potential ($E_{1/2}$) of 0.88 V, both higher than commercial Pt/C ($E_{onset}$: 0.95 V, $E_{1/2}$: 0.85 V), and even superior to most of non-noble ORR catalysts (Table S1 in the ESM). By comparison, C-ZIF shows unsatisfactory ORR activity, while the raw $LiFePO_4$ (LFP) and C-LFP almost have no ORR activity, indicating that the original $LiFePO_4$ is not suitable as an oxygen reduction catalyst. Meanwhile, electrochemical impedance spectroscopy (EIS) results also show that the electron transfer resistance ($R_{ct}$) of C-LFP is much larger than that of C-ZIF/LFP (Fig. S8 in the ESM). This further demonstrates that the unreacted $LiFePO_4$ (C-LFP) remained in C-ZIF/LFP cannot be the oxygen reduction active site. These also manifest that the interatomic recombination between ZIF-8 and $LiFePO_4$ at high temperatures can form active sites that facilitate oxygen reduction. In addition, the Tafel slope of the C-ZIF/LFP (70 mV·$dec^{-1}$) is smaller than commercial Pt/C (75 mV·$dec^{-1}$) (Fig. 4(c)), and its oxygen reduction is performed by an almost four-electron path on the basis of Koutecky-Levich (K-L) formula (Figs. S9 and S10 in the ESM). Interestingly, C-ZIF/LFP exhibits a lower $H_2O_2$% yield compared to commercial Pt/C from 0.6 to 0.8 V (Fig. 4(d)), indicating it keeps higher four-electron reaction efficiency than commercial Pt/C. These demonstrate that C-ZIF/LFP has faster oxygen reduction kinetics. In the subsequent durability and stability test, the current density of C-ZIF/LFP only slightly decreases under long time continuous chronoamperometric measurements for 10 h (Fig. S11 in the ESM). Besides, the current density and

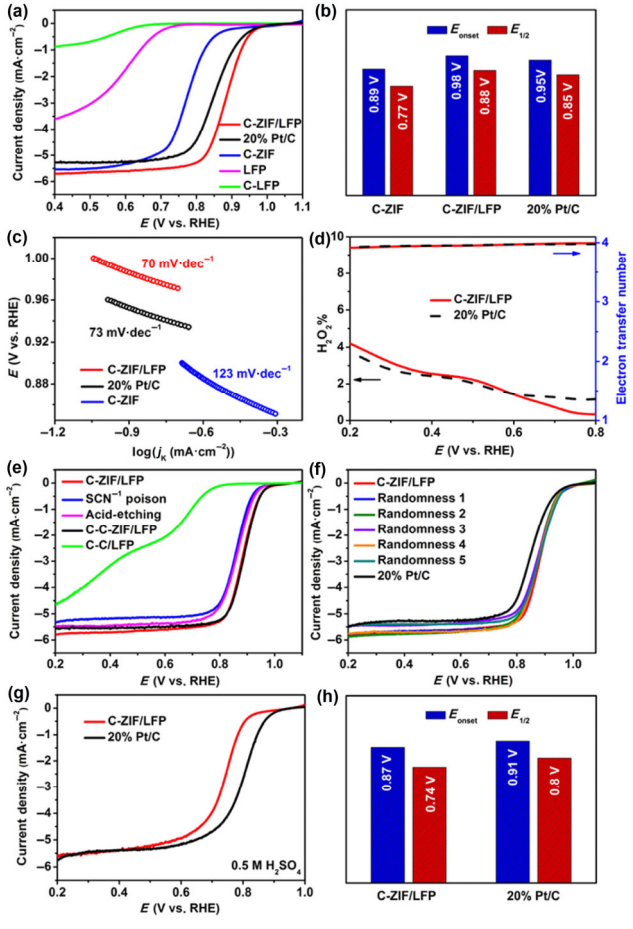


**Figure 4** (a) ORR activity comparison. In 0.1 M KOH (b) $E_{onset}$ and $E_{1/2}$ comparison, (c) Tafel slopes, (d) $H_2O_2$% yield and electron transfer number, (e) active sites exploration, and (f) ORR activity of randomly selected samples from the mass-production catalysts. In 0.5 M $H_2SO_4$ (g) ORR activity comparison and (h) $E_{onset}$ and $E_{1/2}$ comparison.

ORR activity of C-ZIF/LFP remain unchanged before and after the addition of methanol (Figs. S12 and S13 in the ESM). These disclose that C-ZIF/LFP is powerful in terms of stability and methanol resistance.

To explore the active center, C-ZIF/LFP was poisoned by KSCN. In Fig. 4(e), the ORR activity of C-ZIF/LFP is decrease after poisoned by KSCN, which reveals that the N provided by ZIF-8 and the Fe provided by $LiFePO_4$ could be connected together to generate Fe-$N_x$ oxygen reduction active site at high temperatures. Additionally, the ORR activity of C-ZIF/LFP is similarly reduced when it is acid-etched to remove part of $Fe_2P$ (Fig. S14 in the ESM), indicating that $Fe_2P$ has a positive role in assisting the ORR activity of C-ZIF/LFP. Then, when compared the activity of C-C-ZIF/LFP (derived from the mixture of $LiFePO_4$ and nitrogen-containing carbon) and C-C/LFP (derived from the mixture of $LiFePO_4$ and nitrogen-free conductive carbon), C-C-ZIF/LFP is found to exhibit the similar ORR activity as C-ZIF/LFP, while C-C/LFP is almost inactive. Notably, the morphology of C-C-ZIF/LFP and C-C/LFP is similar (a mixture of carbon materials and particles) (Fig. S15 in the ESM), but the phase composition is different (Fig. S16 in the ESM). XRD patterns show that C-C/LFP only has carbon and C-LFP, but there is additional $Fe_2P$ formed in C-C-ZIF/LFP, which not only indicates that $Fe_2P$ has ORR activity, but also proves that N atoms play an important role on the formation of ORR active sites in the final catalyst. Therefore, C-ZIF/LFP shows such excellent ORR activity, not only due to the high conductivity and transport channels provided by coral-like carbon nanotube arrays, but also owing to the synergistic effect of multiple ORR active sites (C-N, P-C, $Fe_2P$ and Fe-Nx) in C-ZIF/LFP.

Furthermore, ZIF-8 was mixed with different amounts of $LiFePO_4$ for calcination, although the activity is not further improved, they are still superior to commercial Pt/C (Fig. S17 in the ESM). Meanwhile, batches of C-ZIF/LFP were produced (Fig. S18 in the ESM), regardless of the state of the precursor mixing, randomly selected samples on the as-prepared catalysts all have better ORR activity than commercial Pt/C, and only with slight difference (Fig. 4(f)). Therefore, it is shown that ZIF-8 and $LiFePO_4$ can be perfectly combined at high temperatures to produce active sites that facilitate oxygen reduction, and this method of preparing high performance ORR catalysts is more suitable for mass production in practical applications.

In 0.5 M $H_2SO_4$ electrolytes, the $E_{1/2}$ of C-ZIF/LFP is 0.74 V, slightly different from commercial Pt/C ($E_{1/2}$: 0.8 V) (Figs. 4(g) and 4(h)). Then in the RRDE test, the $H_2O_2$% yield of C-ZIF/LFP is below 3% (Fig. S19 in the ESM), suggesting the ORR path of C-ZIF/LFP is close to the four-electron transfer path under the acidic electrolytes, consistent with the calculated number of transferred electrons based on K-L formula (Figs. S20 and S21 in the ESM). Besides, it also exhibits better durability and methanol resistance than commercial Pt/C under acidic conditions (Figs. S22 and S23 in the ESM).

Subsequently, C-ZIF/LFP was assembled as the cathode into a Zn-air battery (Fig. 5(a)). First, under liquid electrolyte conditions, the assembled battery owns an open circuit voltage (OCP) of 1.5 V, and the peak power density can reach 140 mW·cm$^{-2}$ (Fig. 5(b) and Fig. S24 in the ESM). Afterwards, the batteries are discharged at 5 and 20 mA, respectively (Figs. 5(c) and Fig. S25 in the ESM). Compared with commercial Pt/C, C-ZIF/LFP always shows higher discharge voltage. Meanwhile, when the C-ZIF/LFP battery is completely discharged, the specific density is calculated to be 792 mAh·$g_{Zn}^{-1}$ based on the mass of zinc foil consumed (Fig. S26 in the ESM). Then, C-ZIF/LFP was further assembled into the solid-state Zn-air battery, whose OCP can still reach 1.39 V, and three such batteries in series can illuminate a ~ 3 V LED bulbs (Fig. 5(d)).

## 4 Conclusions

In summary, we firstly use $LiFePO_4$ as Fe and P sources to prepare coral-like carbon nanotube arrays at high-temperature

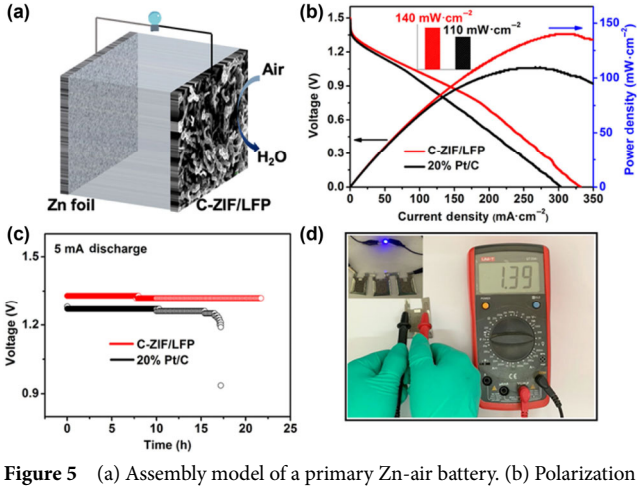


**Figure 5** (a) Assembly model of a primary Zn-air battery. (b) Polarization and power density curves. (c) Discharge curves at 5 mA of C-ZIF/LFP and Pt/C. (d) Open circuit voltage photo of the all-solid-state Zn-air battery assembled using C-ZIF/LFP as cathode (inset: a lighted LED powered by three batteries in series).

treatments by reacting with ZIF-8. Fe and P atoms provided by $LiFePO_4$ and N atom provided by ZIF-8 are mutually incorporated into the carbon framework to synergistically promote oxygen reduction. The obtained catalyst shows superior oxygen reduction performance under both alkaline and acidic conditions, and achieves a high peak power density in Zn-air batteries. More importantly, this work demonstrates that $LiFePO_4$ can serve as both Fe and P sources to prepare high-performance ORR catalysts. Therefore, in this work we put forward a new field for the waste utilization, and propose a new research direction for the high-value recycling of $LiFePO_4$ and even other lithium battery cathode materials.

## Acknowledgements

This work was financially supported by the National Key Research and Development Program of China (No. 2016YFA0202603) and the National Natural Science Foundation of China (No. 51672204).

**Electronic Supplementary Material**: Supplementary material (calculation formula of electron transfer number and hydrogen peroxide yield, SEM images, XRD pattern, TG-DSC curves, CV curves, LSV curves, Koutecky-Levich plots, chronoamperometric responses curves, open-circuit potential plot of Zn-air battery, discharge curves of Zn-air battery and table for ORR activity comparison of non-noble catalysts) is available in the online version of this article at https://doi.org/10.1007/s12274-020-2702-3.

## References

[1] Zhang, L. Z.; Fischer, J. M. T. A.; Jia, Y.; Yan, X. C.; Xu, W.; Wang, X. Y.; Chen, J.; Yang, D. J.; Liu, H. W.; Zhuang, L. Z. et al. Coordination of atomic Co-Pt coupling species at carbon defects as active sites for oxygen reduction reaction. *J. Am. Chem. Soc.* **2018**, *140*, 10757–10763.

[2] Tian, X. L.; Zhao, X.; Su, Y. Q.; Wang, L. J.; Wang, H. M.; Dang, D.; Chi, B.; Liu, H. F.; Hensen, E. J. M.; Lou, X. W. et al. Engineering bunched Pt-Ni alloy nanocages for efficient oxygen reduction in practical fuel cells. *Science* **2019**, *366*, 850–856.

[3] Liu, J.; Jiao, M. G.; Mei, B. B.; Tong, Y. X.; Li, Y. P.; Ruan, M. B.; Song, P.; Sun, G. Q.; Jiang, L. H.; Wang, Y. et al. Carbon-supported divacancy-anchored platinum single-atom electrocatalysts with superhigh Pt utilization for the oxygen reduction reaction. *Angew. Chem., Int. Ed.* **2019**, *131*, 1175–1179.

[4] Tao, L.; Qiao, M.; Jin, R.; Li, Y.; Xiao, Z. H.; Wang, Y. Q.; Zhang, N. N.; Xie, C.; He, Q. G.; Jiang, D. C. et al. Bridging the surface charge and catalytic activity of a defective carbon electrocatalyst. *Angew. Chem., Int. Ed.* **2019**, *131*, 1031–1036.

[5] Tang, C.; Zhong, L.; Zhang, B. S.; Wang, H. F.; Zhang, Q. 3D mesoporous van der waals heterostructures for trifunctional energy electrocatalysis. *Adv. Mater.* **2018**, *30*, 1705110.

[6] Li, Y. B.; Zhong, C.; Liu, J.; Zeng, X. Q.; Qu, S. X.; Han, X. P.; Deng, Y. D.; Hu, W. B.; Lu, J. Atomically thin mesoporous $Co_3O_4$ layers strongly coupled with N-rGO nanosheets as high-performance bifunctional catalysts for 1D knittable zinc-air batteries. *Adv. Mater.* **2018**, *30*, 1703657.

[7] Cheng, H.; Li, M. L.; Su, C. Y.; Li, N.; Liu, Z. Q. Cu-Co bimetallic oxide quantum dot decorated nitrogen-doped carbon nanotubes: A high-efficiency bifunctional oxygen electrode for Zn-air batteries. *Adv. Funct. Mater.* **2017**, *27*, 1701833.

[8] Guo, D. H.; Shibuya, R.; Akiba, C.; Saji, S.; Kondo, T.; Nakamura, J. Active sites of nitrogen-doped carbon materials for oxygen reduction reaction clarified using model catalysts. *Science* **2016**, *351*, 361–365.

[9] Gong, K. P.; Du, F.; Xia, Z. H.; Durstock, M.; Dai, L. M. Nitrogen-doped carbon nanotube arrays with high electrocatalytic activity for oxygen reduction. *Science* **2009**, *323*, 760–764.

[10] Xue, W. D.; Zhou, Q. X.; Li, F. X.; Ondon, B. S. Zeolitic imidazolate framework-8 (ZIF-8) as robust catalyst for oxygen reduction reaction in microbial fuel cells. *J. Power Sources* **2019**, 423, 9–17.

[11] Wang, Q. C.; Ji, Y. J.; Lei, Y. P.; Wang, Y. B.; Wang, Y. D.; Li, Y. Y.; Wang, S. Y. Pyridinic-N-dominated doped defective graphene as a superior oxygen electrocatalyst for ultrahigh-energy-density Zn-air batteries. *ACS Energy Lett.* **2018**, *3*, 1183–1191.

[12] Liu, X.; Liu, H.; Chen, C.; Zou, L. L.; Li, Y.; Zhang, Q.; Yang, B.; Zou, Z. Q.; Yang, H. $Fe_2N$ nanoparticles boosting $FeN_x$ moieties for highly efficient oxygen reduction reaction in Fe-N-C porous catalyst. *Nano Res.* **2019**, *12*, 1651–1657.

[13] Han, Y. H.; Wang, Y. G.; Xu, R. R.; Chen, W. X.; Zheng, L. R.; Han, A. J.; Zhu, Y. Q.; Zhang, J.; Zhang, H. B.; Luo, J. et al. Electronic structure engineering to boost oxygen reduction activity by controlling the coordination of the central metal. *Energy Environ. Sci.* **2018**, *11*, 2348–2352.

[14] Kumar, K.; Gairola, P.; Lions, M.; Ranjbar-Sahraie, N.; Mermoux, M.; Dubau, L.; Zitolo, A.; Jaouen, F.; Maillard, F. Physical and chemical considerations for improving catalytic activity and stability of non-precious-metal oxygen reduction reaction catalysts. *ACS Catal.* **2018**, *8*, 11264–11276.

[15] Wei, W.; Shi, X. M.; Gao, P.; Wang, S. S.; Hu, W.; Zhao, X. X.; Ni, Y. M.; Xu, X. Y.; Xu, Y. Q.; Yan, W. S. et al. Well-elaborated, mechanochemically synthesized Fe-TPP⊂ZIF precursors (Fe-TPP = tetraphenylporphine iron) to atomically dispersed iron-nitrogen species for oxygen reduction reaction and Zn-air batteries. *Nano Energy* **2018**, *52*, 29–37.

[16] Galiote, N. A.; Oliveira, F. E. R.; Lima, F. H. B. FeCo-N-C oxygen reduction electrocatalysts: Activity of the different compounds produced during the synthesis via pyrolysis. *Appl. Catal. B: Environ.* **2019**, *253*, 300–308.

[17] Su, C. Y.; Cheng, H.; Li, W.; Liu, Z. Q.; Li, N; Hou, Z. F.; Bai, F. Q.; Zhang, H. X.; Ma, T. Y. Atomic modulation of FeCo-nitrogen-carbon bifunctional oxygen electrodes for rechargeable and flexible all-solid-state zinc-air battery. *Adv. Energy Mater.* **2017**, *7*, 1602420.

[18] Huang, Z.; Pan, H. Y.; Yang, W. J.; Zhou, H. H.; Gao, N.; Fu, C. P.; Li, S. C.; Li, H. X.; Kuang, Y. F. *In situ* self-template synthesis of Fe-N-doped double-shelled hollow carbon microspheres for oxygen reduction reaction. *ACS Nano* **2018**, *12*, 208–216.

[19] Jiao, L.; Wan, G.; Zhang, R.; Zhou, H.; Yu, S. H.; Jiang, H. L. From metal-organic frameworks to single-atom Fe implanted N-doped porous carbons: Efficient oxygen reduction in both alkaline and acidic media. *Angew. Chem., Int. Ed.* **2018**, *57*, 8525–8529.

[20] Wu, M. M.; Wang, K.; Yi, M.; Tong, Y. X.; Wang, Y.; Song, S. Q. A facile activation strategy for an MOF-derived metal-free oxygen reduction reaction catalyst: Direct access to optimized pore structure and nitrogen species. *ACS Catal.* **2017**, *7*, 6082–6088.

[21] Shui, J. L.; Chen, C.; Grabstanowicz, L.; Zhao, D.; Liu, D. J. Highly efficient nonprecious metal catalyst prepared with metal-organic framework in a continuous carbon nanofibrous network. *Proc. Natl. Accad. Sci. USA* **2015**, *112*, 10629–10634.

[22] Jiao, L.; Wang, Y.; Jiang, H. J.; Xu, Q. Metal-organic frameworks as platforms for catalytic applications. *Adv. Mater.* **2018**, *30*, 1703663.

[23] Aiyappa, H. B.; Masa, J.; Andronescu, C.; Muhler, M.; Fischer, R. A.; Schuhmann, W. MOFs for electrocatalysis: From serendipity to design strategies. *Small Methods* **2019**, *3*, 1800415.

[24] Ma, L. T.; Chen, S. M.; Pei, Z. X.; Huang, Y.; Liang, G. J.; Mo, F. N.; Yang, Q.; Su, J.; Gao, Y. H.; Zapien, J. A. et al. Single-site active iron-based bifunctional oxygen catalyst for a compressible and rechargeable zinc-air battery. *ACS Nano* **2018**, *12*, 1949–1958.

[25] Pendashteh, A.; Vilela, S. M. F.; Krivtsov, I.; Ávila-Brande, D.; Palma, J.; Horcajada, P.; Marcilla, R. Bimetal zeolitic imidazolate framework (ZIF-9) derived nitrogen-doped porous carbon as efficient oxygen electrocatalysts for rechargeable Zn-air batteries. *J. Power Sources* **2019**, *427*, 299–308.

[26] Sun, X. P.; Sun, S. X.; Gu, S. Q.; Liang, Z. F.; Zhang, J. X.; Yang, Y. Q.; Deng, Z.; Wei, P.; Peng, J.; Xu, Y. et al. High-performance single atom bifunctional oxygen catalysts derived from ZIF-67 superstructures. *Nano Energy* **2019**, *61*, 245–250.

[27] Chong, L. N.; Wen, J. G.; Kubal, J.; Sen, F. G.; Zou, J. X.; Greeley, J.; Chan, M.; Barkholtz, H.; Ding, W. J.; Liu, D. J. Ultralow-loading platinum-cobalt fuel cell catalysts derived from imidazolate frameworks. *Science* **2018**, *362*, 1276–1281.

[28] Wang, Z. H.; Jin, H. H.; Meng, T.; Liao, K.; Meng, W. Q.; Yang, J. L.; He, D. P.; Xiong, Y. L.; Mu, S. C. Fe, Cu-coordinated ZIF-derived carbon framework for efficient oxygen reduction reaction and zinc-air batteries. *Adv. Funct. Mater.* **2018**, *28*, 1802596.

[29] Sun, Z. C.; Zhu, M. S.; Lv, X. S.; Liu, Y. Y.; Shi, C.; Dai, Y.; Wang, A. J.; Majima, T. Insight into iron group transition metal phosphides ($Fe_2P$, $Co_2P$, $Ni_2P$) for improving photocatalytic hydrogen generation. *Appl. Catal. B: Environ.* **2019**, *246*, 330–336.

[30] Fan, H. L.; Liu, H.; Hu, X.; Lv, G. Q.; Zheng, Y.; He, F.; Ma, D. L.; Liu, Q.; Lu, Y. Z.; Shen, W. Z. $Fe_2P$@mesoporous carbon nanosheets synthesized via an organic template method as A cathode electrocatalyst for Zn-air batteries. *J. Mater. Chem. A* **2019**, *7*, 11321–11330.

[31] Zhou, B. L.; Yan, F.; Li, X. J.; Zhou, J.; Zhang, W. F. An interpenetrating porous organic polymer as a precursor for FeP/$Fe_2P$-embedded porous carbon toward a pH-universal ORR catalyst. *ChemSusChem* **2019**, *12*, 915–923.

[32] Miao, Z. P.; Wang, X. M.; Tsai, M. C.; Jin, Q. Q.; Liang, J. S.; Ma, F.; Wang, T. Y.; Zheng, S. J.; Hwang, B. J.; Huang, Y. H. et al. Atomically dispersed Fe-$N_x$/C electrocatalyst boosts oxygen catalysis via a new metal-organic polymer supramolecule strategy. *Adv. Energy Mater.* **2018**, *8*, 1801226.

[33] Wu, K. L.; Chen, X.; Liu, S. J.; Pan, Y.; Cheong, W. C.; Zhu, W.; Cao, X.; Shen, R. A.; Chen, W. X.; Luo, J. et al. Porphyrin-like Fe-$N_4$ sites with sulfur adjustment on hierarchical porous carbon for different rate-determining steps in oxygen reduction reaction. *Nano Res.* **2018**, *11*, 6260–6269.

[34] Chen, S.; Zhao, L. L.; Ma, J. Z.; Wang, Y. Q.; Dai, L. M.; Zhang, J. T. Edge-doping modulation of N, P-codoped porous carbon spheres for high-performance rechargeable Zn-air batteries. *Nano Energy* **2019**, *60*, 536–544.

[35] Zhang, L.; Xiong, J.; Qin, Y. H.; Wang, C. W. Porous N-C catalyst synthesized by pyrolyzing g-$C_3N_4$ embedded in carbon as highly efficient oxygen reduction electrocatalysts for primary Zn-air battery. *Carbon* **2019**, *150*, 475–484.

[36] Yang, D. S.; Song, M. Y.; Singh, K. P.; Yu, J. S. The role of iron in the preparation and oxygen reduction reaction activity of nitrogen-doped carbon. *Chem. Commun.* **2015**, *51*, 2450–2453.

[37] Pu, Z. H.; Zhao, J. H.; Amiinu, I. S.; Li, W. Q.; Wang, M.; He, D. P.; Mu, S. C. A universal synthesis strategy for P-rich noble metal diphosphide-based electrocatalysts for the hydrogen evolution reaction. *Energy Environ. Sci.* **2019**, *12*, 952–957.

[38] Kang, B. K.; Im, S. Y.; Lee, J.; Kwag, S. H.; Kwon, S. B.; Tiruneh, S.; Kim, M. J.; Kim, J. H.; Yang, W. S.; Lim, B. et al. *In-situ* formation of MOF derived mesoporous $Co_3N$/amorphous N-doped carbon nanocubes as an efficient electrocatalytic oxygen evolution reaction. *Nano Res.* **2019**, *12*, 1605–1611.

[39] Wan, X. J.; Wu, R.; Deng, J. H.; Nie, Y.; Chen, S. G.; Ding, W.; Huang, X.; Wei, Z. D. A metal-organic framework derived 3D hierarchical Co/N-doped carbon nanotube/nanoparticle composite as an active electrocatalyst for oxygen reduction in alkaline electrolyte. *J. Mater. Chem. A* **2018**, *6*, 3386–3390.

[40] Liu, S. J.; Amiinu, I. S.; Liu, X. B.; Zhang, J.; Bao, M. J.; Meng, T.; Mu, S. C. Carbon nanotubes intercalated Co/N-doped porous carbon nanosheets as efficient electrocatalyst for oxygen reduction reaction and zinc-air batteries. *Chem. Eng. J.* **2018**, *342*, 163–170.

[41] Jiang, R.; Li, L.; Sheng, T.; Hu, G. F.; Chen, Y. G.; Wang, L. Y. Edge-site engineering of atomically dispersed Fe-$N_4$ by selective C–N bond cleavage for enhanced oxygen reduction reaction activities. *J. Am. Chem. Soc.* **2018**, *140*, 11594–11598.

[42] Wang, J. P.; Han, G. K.; Wang, L. G.; Du, L.; Chen, G. Y.; Gao, Y. Z.; Ma, Y. L.; Du, C. Y.; Cheng, X. Q.; Zuo, P. J. et al. ZIF-8 with ferrocene encapsulated: A promising precursor to single-atom Fe embedded nitrogen-doped carbon as highly efficient catalyst for oxygen electroreduction. *Small* **2018**, *14*, 1704282.

[43] Qin, Q.; Jang, H.; Li, P.; Yuan, B.; Liu, X. E.; Cho, J. A tannic acid-derived N-, P-codoped carbon-supported iron-based nanocomposite as an advanced trifunctional electrocatalyst for the overall water splitting cells and zinc-air batteries. *Adv. Energy Mater.* **2019**, *9*, 1803312.

[44] Wang, R.; Dong, X. Y.; Du, J.; Zhao, J. Y.; Zang, S. Q. MOF-derived bifunctional $Cu_3P$ nanoparticles coated by a N,P-codoped carbon shell for hydrogen evolution and oxygen reduction. *Adv. Mater.* **2018**, *30*, 1703711.

[45] Xue, X. Y.; Yang, H.; Yang, T.; Yuan, P. F.; Li, Q.; Mu, S. C.; Zheng, X. L.; Chi, L. F.; Zhu, J.; Li, Y. G. et al. N,P-coordinated fullerene-like carbon nanostructures with dual active centers toward highly-efficient multi-functional electrocatalysis for $CO_2$RR, ORR and Zn-air battery. *J. Mater. Chem. A* **2019**, *7*, 15271–15277.

[46] Li, Y. H.; Chen, B. X.; Duan, X. Z.; Chen, S. M.; Liu, D. B.; Zang, K. T.; Si, R.; Lou, F. L.; Wang, X. H.; Rønning, M. et al. Atomically dispersed Fe-N-P-C complex electrocatalysts for superior oxygen reduction. *Appl. Catal. B: Environ.* **2019**, *249*, 306–315.

[47] Bi, Z. H.; Huo, L.; Kong, Q. Q.; Li, F.; Chen, J. P.; Ahmad, A.; Wei, X. X.; Xie, L. J.; Chen, C. M. Structural evolution of phosphorus species on graphene with a stabilized electrochemical interface. *ACS Appl. Mater. Interfaces* **2019**, *11*, 11421–11430.